IEEE Access
Multidisciplinary | Rapid Review | Open Access Journal

Received September 15, 2019, accepted September 30, 2019, date of publication October 10, 2019,
date of current version October 28, 2019.

Digital Object Identifier 10.1109/ACCESS.2019.2946859

Low-Loss Wide-Tuning-Range Three-Pole Frequency-Agile Bandpass Diplexer With Identical Constant Absolute Bandwidth

ZHIYOU LI[1], XIAOHONG TANG[1], (Member, IEEE), DI LU[2], (Member, IEEE), ZONGQI CAI[1], YONG LIU[1], AND JUNXIN LUO[3]

[1]School of Electronic Science and Engineering, University of Electronic Science and Technology of China, Chengdu 611731, China
[2]Electronic Engineering Department, The Chinese University of Hong Kong, Hong Kong
[3]Aether Y&D Electronics and Information, Shenzhen 518101, China

Corresponding author: Di Lu (ludi888abc@hotmail.com)

ABSTRACT This paper presents a low-loss, high-isolation and wide-frequency-tuning-range (FTR) (45%) implementation of the three-pole frequency-agile bandpass diplexer (FA-BPD) with identical constant absolute bandwidth (IC.ABW). The FA-BPD includes two three-pole channels and each channel has three transmission zeros (TZs). To develop such a FA-BPD, first, two bandwidth (BW) -identical and -constant frequency-agile bandpass filters (FA-BPFs) with the FTRs of 1.35-2.25 GHz and 1.9-3 GHz are designed individually. Both two FA-BPFs simultaneously employ the cascaded triplet (CT) topology and source-load coupling to introduce three TZs. All couplings of two filters are arranged opposite in sign, thus two TZs of one channel are placed on the side of the other channel. Finally, two FA-BPFs are fed by a common coupling line, thus forming the three-pole 1.35-3-GHz FA-BPD. The design example is fabricated and measured. The experimental results show that the FTRs are 1.35-2.25 GHz (50%) and 1.9-3.0 GHz (44.9%). The ABW of the two channels keeps nearly a constant of 194±8 MHz. The insertion loss (IL) varies within the range of 2.1-3.3 dB. The measured isolation level keeps better than 38 dB.

INDEX TERMS Element variable coupling matrix, frequency-agile bandpass diplexer, identical constant absolute bandwidth.

I. INTRODUCTION

Frequency-agile bandpass diplexer (FA-BPD) applying to the reconfigurable and multiband wireless communication systems have been researched for many years (e.g. [1]–[9]). Some frequency-duplex-division (FDD) transceivers using the same transmitting and receiving bandwidth [1], [2] require the employed FA-BPDs with identical and constant absolute bandwidth (IC.ABW).

To develop such a high-performance FA-BPD, a lot of efforts have been made e.g. in [3]–[9]. A three-pole tunable diplexer with the frequency tuning ranges (FTRs) of 1.43-2.07 GHz (37.3%) and 1.53-2.07 GHz (39%) was demonstrated in [3]. But its insertion loss (IL) was 7.7 dB because of the extra T-junction. In [4], a three-pole tunable diplexer with FTRs of 1.28-1.78 GHz (32.7%) and 2-2.3 GHz (13%) was presented. Its IL was 8.2 dB. In [5], a fourth-order tunable diplexer with the FTRs of 1.2-1.8 GHz (35%) and 2.0-2.6 GHz (26.1%) was proposed. However, the IL was 8.5 dB. A three-pole tunable diplexer with the reconfigurable bandwidth was presented in [6]. It is found that although its IL was very good (2.9 dB), its FTRs were only 25.1% (0.94-1.21 GHz) and 23.5% (1.51-1.91 GHz). A three-pole diplexer with around 50% FTR was presented in [7]. Due to too many varactors used there, the IL was 7.7 dB. The higher-order tunable diplexers employing the classical cascaded trisection (CT) and cascaded quadruplet (CQ) topology were developed in [8] and [9]. However, the IL was 4.9 dB for the tunable diplexer in [8], and the FTR was only 25% for the diplexer in [9].

As can be found, the high-order FA-BPD with IC.ABW is still a big challenge not to mention achieving good IL performance with a wide FTR (e.g. 50%). This is mainly because, as the basic elements of a FA-BPD, the design of two 50%-FTR frequency-agile bandpass filters (FA-BPFs) with CABW and the same bandwidth (BW) at the different frequency is an obstacle even though many FA-BPFs with CABW and wider FTR have been reported (such as in [10]–[20]). To realize these two FA-BPFs, both the design synthesis and realizable structures are indispensable.

The associate editor coordinating the review of this manuscript and approving it for publication was Ali Afana.

This work is licensed under a Creative Commons Attribution 4.0 License. For more information, see http://creativecommons.org/licenses/by/4.0/

A simple and effective tunable filter design methodology has been proposed in [9]. By separately realizing the slope factor matrix $[c]$ and frequency-independent matrix $[m_\Delta]$ of an element variable coupling matrix (EVCM), a FA-BPF can be exclusively implemented from a filter prototype. Following this design methodology, the FA-BPF with different frequency, different BW, different FTR can be realized flexibly, which makes it possible in theory to achieve the two desired FA-BPFs with the same ABW at the different frequency.

This paper presents a new three-pole FA-BPD to realize two low-loss and equal-bandwidth tunable channels with wide FTR and IC.ABW. The presented FA-BPD is constructed by two three-pole filters. They have the same CABW, three TZs, and mirror-symmetric TZ distributions resulting in IC.ABW, high selectivity and good isolation for the diplexer. Since only four varactors are used for each channel, the IL of the diplexer is relatively low. For verification, the diplexer is fabricated and measured. The experimental results show good agreement with simulated ones. The FTRs of two channels are 1.35-2.25 GHz (50%) and 1.9-3.0 GHz (44.9%). The 3dB bandwidth of two channels is kept nearly a constant of 194±8 MHz. In addition, the IL better than 3.3 dB, the isolation higher than 38 dB and three TZs are all the competitive advantages.

The contributions of this paper can be summarized as:

1) The diplexer coupling topology consisting of two mirror-symmetric CT filter topologies is proposed to the application of a FA-BPD design, so as to enhance the isolation level and make the FA-BPD design more straightforward. Although the diplexer topology has been widely used in the frequency-fixed filter design, this is the first realization of a tunable diplexer with an identical and constant absolute bandwidth.
2) Compared to the FA-BPD in [9], this paper proposes a new way to realize the odd-order FA-BPD and is able to implement two tunable and mirror-symmetric responses with three TZs. In the meantime, the proposed three-pole FA-BPD exhibits lower IL and wider FTR.
3) In contrast to the FA-BPD in [8], the proposed FA-BPD realized IC.ABW, wider FTR and lower IL using the advanced coupling matrix and novel structure. Though the proposed FA-BPD has larger circuit size, the presented structure is less complicated and more flexible, which can be used to realize different bandwidth with CABW at the different frequency.

It is also worth mentioning that, [19] presented the single-band second-order FA-BPF based on the synchronously-tuned resonator (STR). However, this paper reports on the diplexer design with two three-pole passband responses and also with mirror-symmetric TZ placement and IC.ABW, even though the used resonator structure is similar.

II. DESIGN AND EXPERIMENTS

To better understand the proposed diplexer, the design theory and the related experimental demonstration in this section

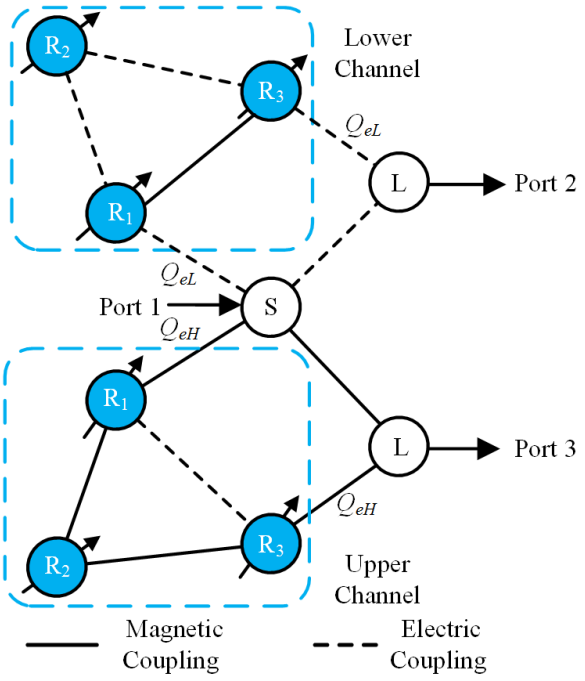

FIGURE 1. Coupling scheme of the proposed three-pole FA-BPD.

are organized as follow. The coupling scheme of the proposed FA-BPD is presented and its ability to improve the isolation between two channels is illustrated in section II-A. Afterward, two types of varactor-tuned resonator used to realize the FA-BPD are presented and investigated in section II-B. Then, the design procedure of the proposed FA-BPD is summarized in Section II-C. Following the procedure, the lower and upper channel of the FA-BPD are designed separately and verified experimentally in Section II-D. Finally, the configuration of FA-BPD is formed by effectively integrating two standalone filters. Experimental demonstration of the final diplexer is carried out and its performance superiorities are confirmed by the measured results in section II-E.

A. COUPLING SCHEME OF FA-BPD

The coupling scheme of the proposed three-pole FA-BPD is presented in Fig. 1. The FA-BPD can be treated as two three-pole cross-coupled FA-BPFs which are fed by a common input. For each channel, source-load coupling and cross-coupling are used simultaneously, while the corresponding couplings of two channels are arranged all opposite in sign. As a result, three TZs will be introduced for each channel and two of them will be placed in the passband of the other channel.

The typical response of a diplexer formed by two three-pole filters is plotted in Fig. 2(a). As shown, the center frequencies of the two channels are 1.95 GHz and 2.2 GHz, respectively, and the isolation level is around 20 dB. The response of the presented diplexer (in Fig. 1) is shown in Fig. 2(b). Obviously, with three prescribed TZs, not only will the frequency selectivity close to the passband

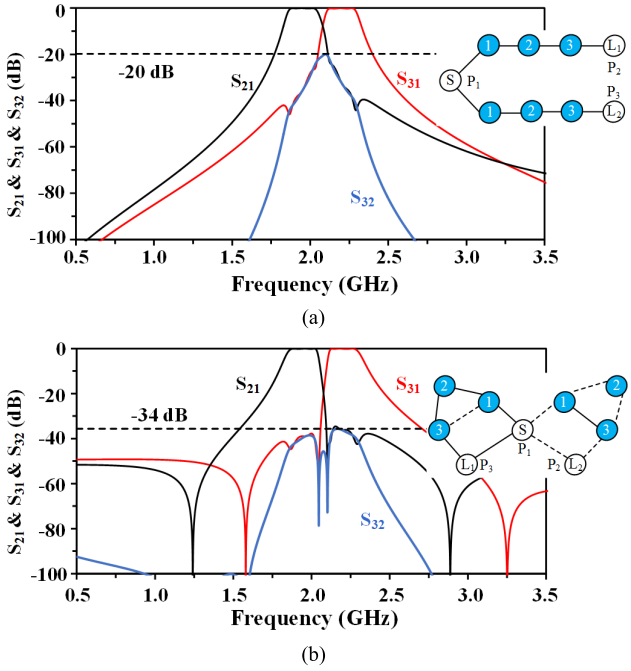

FIGURE 2. Frequency responses of a three-pole fixed-frequency diplexer (a) without TZ and (b) with the prescribed TZs.

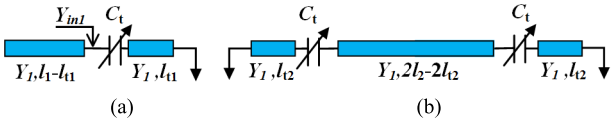

FIGURE 3. (a) QWSTR. (b) HWSTR.

be increased, but the isolation level will also be improved effectively (by around 14 dB).

B. SYNCHRONOUSLY-TUNED RESONATOR

To implement the coupling scheme in Fig. 1, the quarter-wavelength synchronously-tuned resonator(QWSTR) and the half-wavelength synchronously-tuned resonator (HWSTR) are employed, as shown in Fig. 3(a) and (b). QWSTR is used to realize the resonant nodes R_1 and R_3 and HWSTR for the resonant node R_2. The employed varactor model is MA-COM MA46H202 ($C_t = 0.6 \sim 15$ pF, $R_s = 1\ \Omega$) [21] and the substrate is Rogers RT/Duroid 5880 ($h = 0.787$ mm, $\varepsilon_r = 2.2$, $\tan\delta = 0.0009$).

The input admittance of a QWSTR can be derived as:

$$Y_{in1} = jY_1 \tan\beta(l_1 - l_{t1}) + \frac{j2\pi fC_t(-jY_1 \cot\beta l_{t1})}{j2\pi fC_t - jY_1 \cot\beta l_{t1}} \quad (1)$$

For HWSTR, odd-even mode analysis is applied for simplification. Thus, the odd-even equivalent circuits are obtained as shown in Fig. 4. The input admittances can be written as:

$$Y_{in2e} = jY_1 \tan\beta(l_2 - l_{t2}) + \frac{j2\pi fC_t(-jY_1 \cot\beta l_{t2})}{j2\pi fC_t - jY_1 \cot\beta l_{t2}} \quad (2)$$

$$Y_{in2o} = -jY_1 \cot\beta(l_2 - l_{t2}) + \frac{j2\pi fC_t(-jY_1 \cot\beta l_{t2})}{j2\pi fC_t - jY_1 \cot\beta l_{t2}} \quad (3)$$

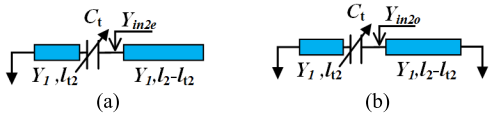

FIGURE 4. HWSTR. (a) Even-mode equivalent circuit. (b) Odd-mode equivalent circuit.

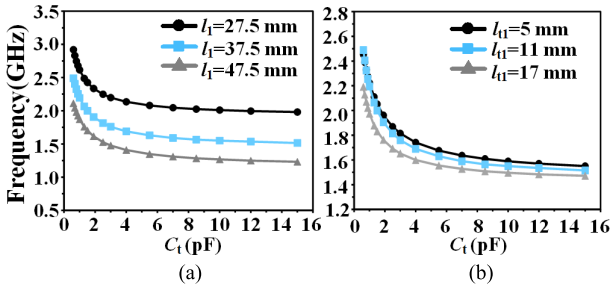

FIGURE 5. Frequency tuning behavior of the QWSTR where $Y_1 = 0.01$ S, (a) with different l_1 where $l_{t1} = 11$ mm, (b) with different l_{t1} where $l_1 = 37.5$ mm.

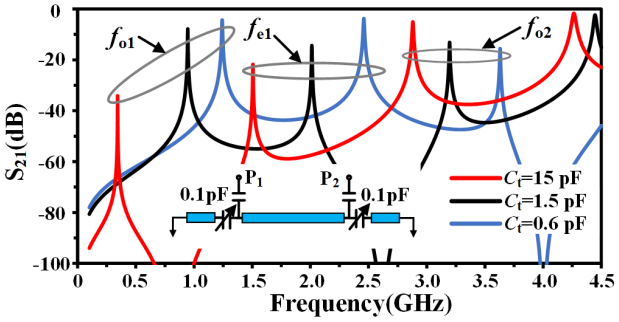

FIGURE 6. Odd/even-mode resonant frequencies of the HWSTR versus the different value of C_t where $l_2 = 37.5$ mm and $l_{t2} = 5$ mm.

Y_1 is characteristic admittance and $\beta = 2\pi/\lambda_g$(λ_g is the guided wavelength). l_i and l_{ti} ($i = 1, 2$) are the physical lengths of the microstrip line. By solving Im (Y_{in1}) = 0, Im (Y_{in2e}) = 0 and Im (Y_{in2o}) = 0, the resonant frequencies of the QWSTR and HWSTR can be obtained. Fig. 5 shows the frequency variation of the QWSTR by tuning C_t. As can be seen, the frequency position of the FTR is mainly decided by the total length l_1 of the resonator, whereas, l_{t1} affects the frequency only a little even though with a very large variation.

The frequency responses of the HWSTR using weak coupling excitation are shown in Fig. 6. Three resonant modes can be found. To form the coupling scheme, only the even-mode resonant frequency is utilized and the odd mode is suppressed by adding a resistor R_c at the center of the resonator [22].

The typical responses of the HWSTR with differentR_c are shown in Fig. 7. With the increase of R_c, the odd mode of the resonator is suppressed gradually. However, the even mode keeps unchanged from beginning to end. The good

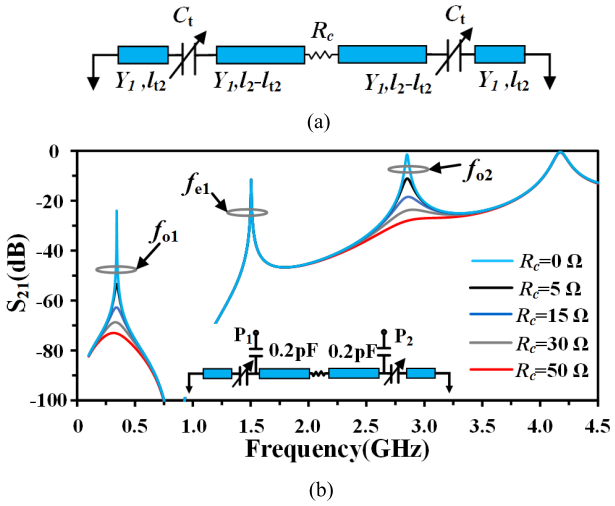

FIGURE 7. (a) HWSTR with the loaded resistor R_c. (b) Frequency responses of the HWSTR with different loaded R_c where $C_t = 15$ pF, $l_2 = 37.5$ mm, $l_{t2} = 5$ mm and using the weak coupling excitation.

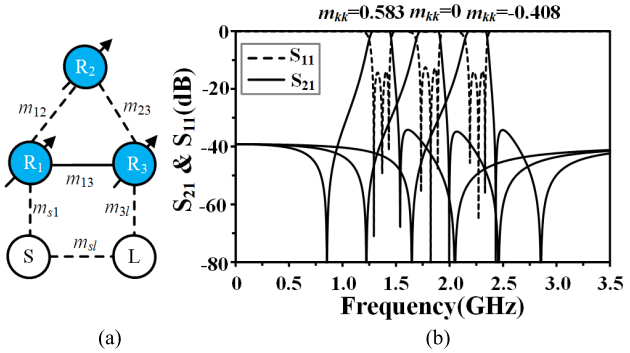

FIGURE 8. (a) Coupling topology of the lower channel filter (solid line is positive and the dash line is negative). (b) Frequency responses of the extracted EVCM for the FA-BPF with CABW where m_{kk} varies from 0.583 to -0.45 at $f_d = 1.8$ GHz.

odd-mode suppression can be obtained when the resistor is 30 Ω (considering the added loss introduced by the resistor).

C. DESIGN PROCEDURE OF THE FA-BPD

To make the FA-BPD design more straightforward, simple and effective design procedures are required. First, since the design of the single channel of the FA-BPD can be roughly treated as the design of two FA-BPFs, EVCM need to be calculated and used to design single-band filter according to [19]. With the EVCMs of the two channels, the coupling coefficients and external quality can be extracted to initiate the layout. The fine optimization process is required to further improve the performance and yield more stable ABW and better RL. Subsequently, the design flow of the proposed FA-BPD can be summarized.

1) FILTER PROTOTYPE FOR THE SINGLE CHANNEL

[19] reported a simple and effective design methodology for FA-BPF with CABW. According to [19], a FA-BPF and its tuning behavior can be uniquely represented and predefined by an element variable coupling matrix (EVCM) as:

$$[m_\Delta]_t = ([m_\Delta] + m_{kk}[c]) \tag{4}$$

$$Q_{et} = \Delta Q_e + m_{kk} c_Q \tag{5}$$

$$m_{kk} = \frac{f_d}{f_t} - \frac{f_t}{f_d} \tag{6}$$

where $[m_\Delta]_t$ is EVCM, $[m_\Delta]$ is the fixed matrix of the $[m_\Delta]_t$, m_{kk} is the self-coupling coefficient, $[c]$ is the slope factor matrix, c_Q is the slope factor for the external quality Q_e, f_d is the mapping frequency and f_t is the tuning center frequency. When the filter is designed according to the predefined EVCM, the filter can be tuned as predicted.

The filter for the lower channel is designed with two TZs that placed at the upper stopband. The FTR and return loss (RL) are predefined as 1.35-2.25 GHz and 15 dB (the equal-ripple bandwidth is 150 MHz). Three TZs are located at -9.5j, 2.5j and 7.6j. The magnetic coupling is set as positive and the electric coupling for negative. The $[m_\Delta]$ and $[c]$ can be obtained according to the method in [19], as:

$$[m_\Delta] = \begin{bmatrix} 0 & -0.0749 & 0.0374 \\ -0.0749 & -0.0490 & -0.0749 \\ 0.0374 & -0.0749 & 0 \end{bmatrix}, \begin{matrix} \Delta Q_e = 13.2 \\ m_{sl} = -4.33e{-}4 \end{matrix} \tag{7}$$

$$[c] = \begin{bmatrix} 1 & -0.0375 & 0.0187 \\ -0.0375 & 0.9755 & -0.0375 \\ 0.0187 & -0.0375 & 1 \end{bmatrix}, \quad c_Q = -6.2 \tag{8}$$

Note that, the diagonal of matrix $[m_\Delta]$ is nonzero because the three-pole cross-coupled filter is asymmetric. The coupling topology and the theoretical frequency responses are presented in Fig. 8. The coupling coefficient m_{13} is magnetic coupling and the others are electric coupling.

The filter for the upper channel of the FA-BPD is designed with two TZs that placed at the lower stopband. The FTR and RL are predefined as 1.9-3.0 GHz and 15 dB (the equal-ripple bandwidth is 150 MHz). Three TZs are located at -9j, 1.9j and 10.4j. The matrix $[m_\Delta]$ and $[c]$ for the filter can be obtained as:

$$[m_\Delta] = \begin{bmatrix} 0 & 0.0499 & -0.0329 \\ 0.0499 & 0.0425 & 0.0499 \\ -0.0329 & 0.0499 & 0 \end{bmatrix}, \begin{matrix} \Delta Q_e = 18.7 \\ m_{sl} = 3.06e-4 \end{matrix} \tag{9}$$

$$[c] = \begin{bmatrix} 1 & 0.025 & -0.0164 \\ 0.025 & 1.0213 & 0.025 \\ -0.0164 & 0.025 & 1 \end{bmatrix}, c_Q = -8.89 \tag{10}$$

The coupling topology and frequency responses of the EVCM are shown in Fig. 9. The coupling coefficient m_{13} is electric coupling and the others are magnetic coupling.

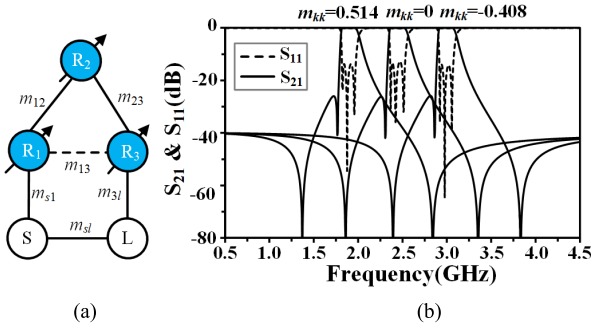

FIGURE 9. (a) Coupling topology the upper channel filter. (b) Frequency responses of the extracted EVCM for the FA-BPF with CABW where m_{kk} varies from 0.514 to -0.408 at f_d = 2.45 GHz.

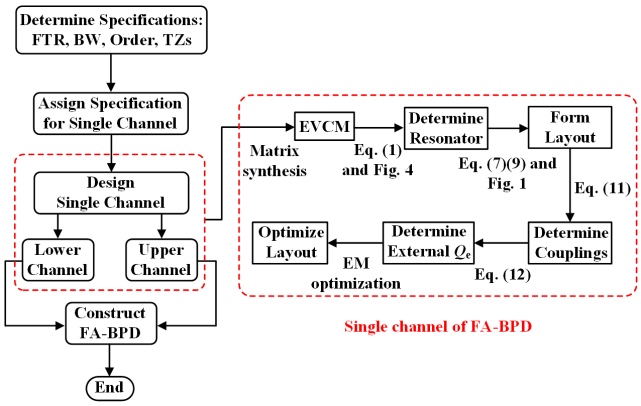

FIGURE 10. The design flow chart of the FA-BPD.

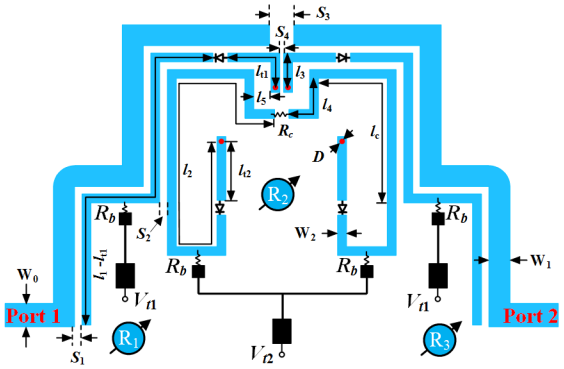

FIGURE 11. Layout of the lower channel.

2) COUPLING COEFFICIENTS AND EXTERNAL QUALITY

According to the method in [22], the coupling coefficient between two resonators can be extracted by:

$$m_{ij} = \pm\frac{1}{2}\left(\frac{f_{02}}{f_{01}}+\frac{f_{01}}{f_{02}}\right)\sqrt{\left(\frac{f_2^2-f_1^2}{f_2^2+f_1^2}\right)^2-\left(\frac{f_{02}^2-f_{01}^2}{f_{02}^2+f_{01}^2}\right)^2} \tag{11}$$

where f_1 and f_2 are the characteristic frequencies of two coupled resonators. f_{01} and f_{02} are the self-resonant frequencies.

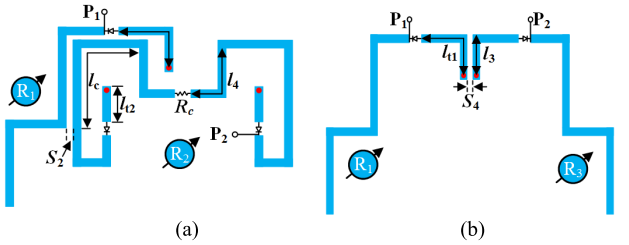

FIGURE 12. Circuit models for extracting (a) m_{12} and (b) m_{13} of the lower channel.

To realize the external quality Q_e in EVCM of the two channels, the parallel coupling feed-line is utilized. The Q_e is extracted according to the method in [22] as:

$$Q_e = \frac{\pi f_0 \tau_{s11}(f_0)}{2} \tag{12}$$

where f_0 is the resonant frequency and τ_{s11} is the group delay of S_{11} at f_0.

3) OPTIMIZATION

Based on the extracted coupling coefficient and Q_e curves, the dimensions of the single-channel filter can be roughly initiated. However, the FTR of the resonator, external quality, and coupling coefficients are hard to perfectly match the desired values due to the nature of the filter structures. Thus, the optimization process is needed. For instance, to correct the FTR, the resonator length needs to be slightly adjusted. The RL can be optimized by adjusting the width of the feeding line and the coupling gap. The bandwidth fluctuation can be minimized by slightly changing the coupling zone of the two adjacent resonators and employing two different capacitance values.

4) DESIGN FLOW OF THE FA-BPD

With the EVCMs and the equations above, the design flow of the FA-BPD can be summarized as follows:

(a) Determine the specifications of the FA-BPD including the order, bandwidth, FTR, RL and the number of TZs.
(b) Determine the specifications of the two single channels, and obtain the EVCMs according to the method in [19].
(c) Initiate the dimensions of the QWSTR and HWSTR based on Eq. (1) and the frequency tuning curves in Fig. 4.
(d) Determine the feeding structure at the common port, and form the layout of the two single channels based on Eq. (7), Eq. (9) and the coupling topology in Fig. 1.
(e) Extract and determine the couplings between two resonators based on Eq. (11).
(f) Extract and determine the external Q_e of each channel based on Eq. (12).
(g) Optimize the layout of each channel to approach the desired frequency response.
(h) Integrate the two single channels and construct the desired FA-BPD.

The design flow chart is given in Fig. 10.

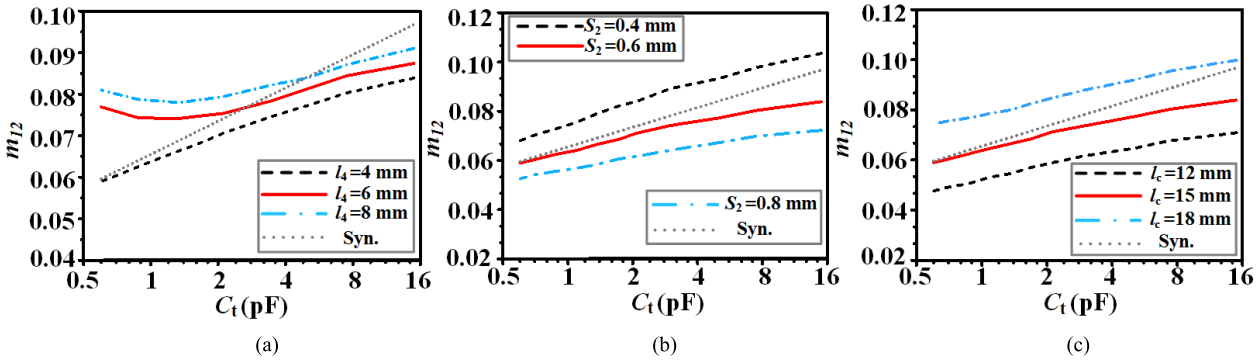

FIGURE 13. Coupling coefficient m_{12} versus C_t with different (a) l_4 when $S_2 = 0.6$ mm, $l_c = 15$ mm, (b) S_2 when $l_4 = 4$ mm, $l_c = 15$ mm, (c) l_c when $l_4 = 4$ mm, $S_2 = 0.6$ mm.

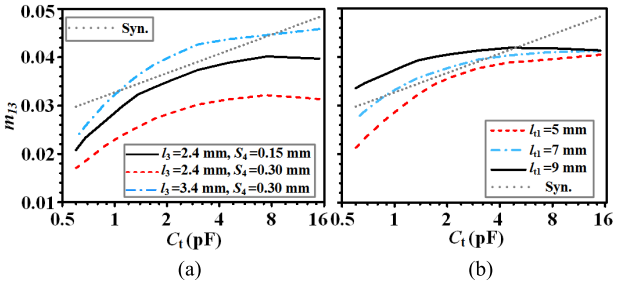

FIGURE 14. Coupling coefficients m_{13} versus C_t with (a) $l_3 = 2.4$ mm, $S_4 = 0.15$ mm; $l_3 = 2.4$ mm, $S_4 = 0.3$ mm; $l_3 = 3.4$ mm, $S_4 = 0.3$ mm; and (b) different l_{t1} when $l_3 = 2.4$ mm, $S_4 = 0.15$ mm.

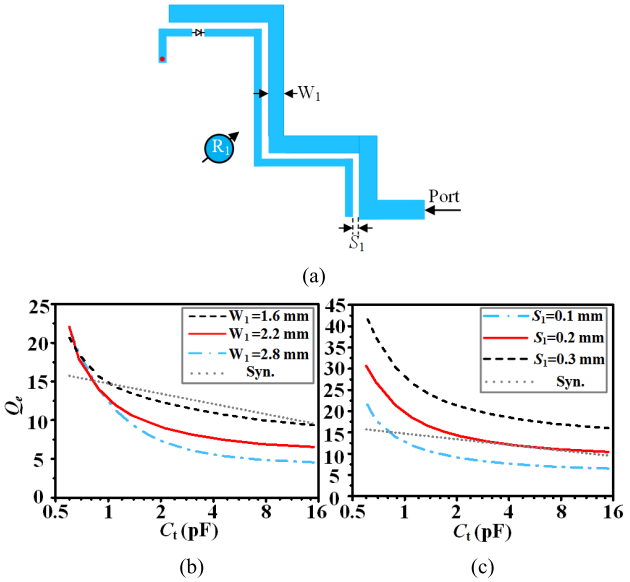

FIGURE 15. (a) Circuit models for extracting Q_e. (b) Q_e versus C_t with different values of W_1 when $S_1 = 0.1$ mm. (c) Q_e versus C_t with different values of S_1 when $W_1 = 2.2$ mm.

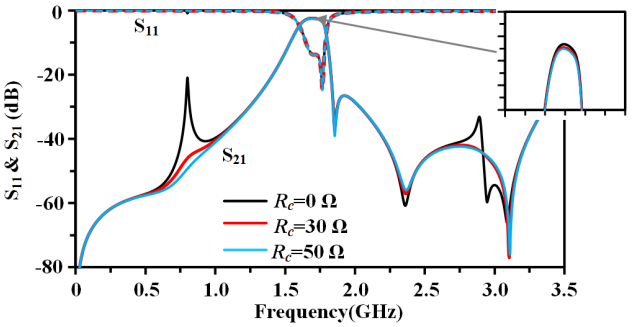

FIGURE 16. The simulated frequency response with different R_c at 1.6 GHz.

D. DESIGN OF THE SINGLE CHANNEL OF THE FA-BPD

1) LOWER CHANNEL

Fig. 11 presents the lower channel of the FA-BPD to realize the coupling topology in Fig. 8(a). As shown, it consists of two QWSTRs and a HWSTR which are used to realize the resonant nodes R_1, R_3 and R_2 in Fig. 8(a).

Following the aforementioned design procedure, the coupling coefficient curves of the filter are extracted based on Eq. (11). The models for extracting the coupling coefficients are presented in Fig. 12.

The curves of coupling coefficient m_{12} are plotted in Fig. 13 when C_t varies from 0.6 pF to 15 pF. It is found, the m_{12} curve in EVCM can be realized in this way. At first, changing l_4 makes the variation slope of m_{12} to be a linear function. Then, selecting the proper S_2 obtains the desired variation slope with the linear function unchanged. Finally, adjusting l_c obtains the desired m_{12} curve position with nearly unchanged curve shape. Thus, the m_{12} function in EVCM is realized approximately.

The m_{13} curves with different dimension parameters are plotted in Fig. 14. Accordingly, choosing the appropriate l_3 and S_4 predefines m_{13} in the low-frequency area. Then, choosing l_{t1} predefines m_{13} in the high-frequency area. Using this method, the m_{13} function in EVCM can be achieved. As shown in Fig. 11, the desired source-load coupling m_{sl} is obtained by choosing proper S_3.

When the required m_{13} is obtained, the l_{t1} is determined. The external quality Q_e is extracted based on Eq. (12) and the circuit model in Fig. 15(a). As shown in Fig. 15(b) and (c), choosing the appropriate W_1 yields the appropriate variation

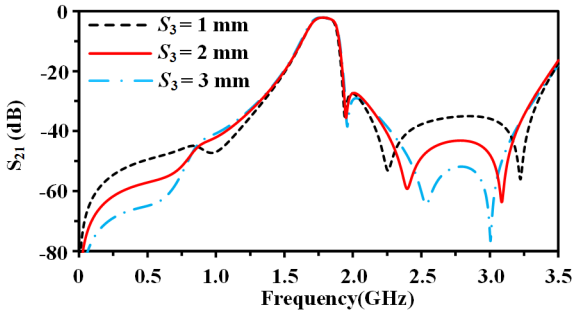

FIGURE 17. The typical frequency response of the lower channel with different S_3 at 1.8 GHz.

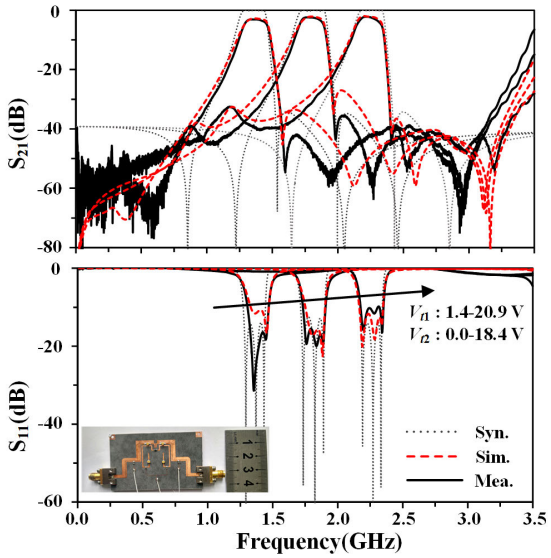

FIGURE 18. Synthesized, simulated and measured frequency responses of the lower channel with the photograph. ($\tan\delta = 0.0009$, $R_S = 1\ \Omega$).

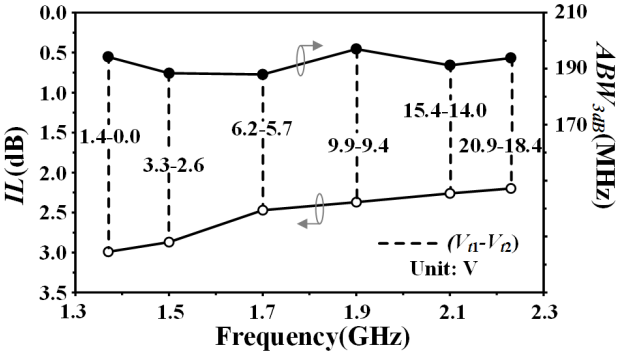

FIGURE 19. Measured IL and 3dB-BW of the lower channel.

TABLE 1. The initial and optimized physical dimensions of the lower channel (unit: mm).

	$W_0/W_1/W_2$	$S_1/S_2/S_3$ /S_4	$l_1/l_2/l_3/l_4/l_5$/ $l_{t1}/l_{t2}/l_c$	D
Init.	2.4/1.6/0.72	0.1/0.6/1 /0.3	47.5/45/3.4/6/2 /11/11/15	0.4
Opt.	2.4/2.2/0.72	0.2/0.73/1.8 /0.15	45/41/2.8/4.925/1.38 /6.28/6/16.855	0.4

TABLE 2. The capacitance values and control voltages for the lower channel.

Freq.(GHz)	C_{t1}(pF)	C_{t2}(pF)	V_{t1}(V)	V_{t2}(V)
1.35	7.5	15	1.4	0.0
1.8	1.74	1.77	7.9	7.4
2.25	0.7	0.7	20.9	18.4

slope of Q_e curve, and then changing S_1 determines the value of Q_e. In this way, the Q_e in EVCM can be obtained.

Adding resistor R_c to HWSTR will suppress spurious resonance. As shown in Fig. 16, the IL will degrade with the increases of R_c. However, the suppression level will keep almost unchanged when R_c is over 30 Ω, which is in accordance with the simulation results in Fig. 7 and confirms the optimum $R_c = 30\ \Omega$.

The key parameters of the layout are initiated. Afterward, the filter is optimized using ADS and HFSS. The whole optimization process is summarized as: first, adjusting l_4 and l_5 changes the coupling zone of resonator 1 and 2 to stabilize the ABW. Then, the varactor loading position l_{t1} and l_{t2} are optimized to improve RL over the entire FTR. However, the change of l_{t1} and l_{t2} causes the small shifts of FTR, m_{12} and m_{13}. Therefore, l_1 and l_2 are adjusted to move back the FTR. The m_{12} is corrected by adjusting l_c, l_4 and S_2. The m_{13} is corrected by adjusting l_3 and S_4. Then, the source-load coupling is decided by choosing a proper S_3. As illustrated in Fig. 17, the TZ is moved close to the passband as S_3 decreases. Through a few iterations of this optimization process, the optimized dimensions are obtained and listed in Table 1 which are comparing with the initial values.

For verification, the filter is fabricated and measured using the Keysight VNA N5235A. The measured, simulated and synthesized results with its photograph are shown in Fig. 18. The bias resistor R_b is 100 kΩ. The 30-Ω resistor is added at the center of the HWSTR. To control the FA-BPF, the bias voltages V_{t1} from 1.4 V to 20.9 V and V_{t2} from 0.0 V to 18.4 V are applied. As shown in Fig. 18, the measured results agree well with the simulated results and reasonably match the synthesized results. The filter is tuned within the FTR of 1.35-2.25 GHz (50%) and with a constant 3dB-BW of 192.5±4.5 MHz. The IL varies from 2.2 to 2.9 dB. Two TZs generated in the upper stopband effectively enhances the upper stopband suppression and sharpens the skirt of the passband. Since the spurious odd mode of the HWSTR is not completely suppressed by the loading resistor, the suppression level in the lower stopband gradually increases and the lower-frequency TZ disappears when the frequency is tuned high. The measured 3dB-BW and IL performance are summarized in Fig. 19. The control voltages and capacitance values are listed in Table 2. C_{t1} and C_{t2} with a slight difference are used to obtain better RL.

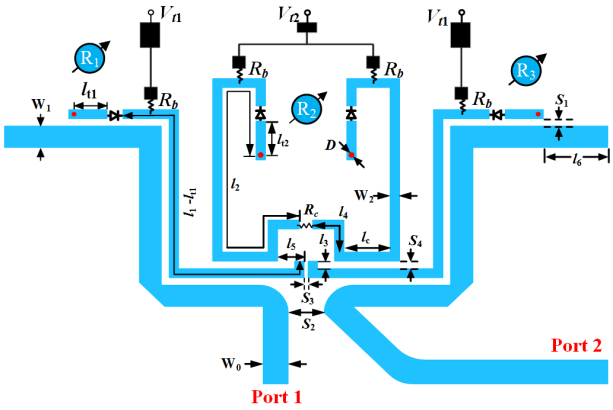

FIGURE 20. Layout of the upper channel.

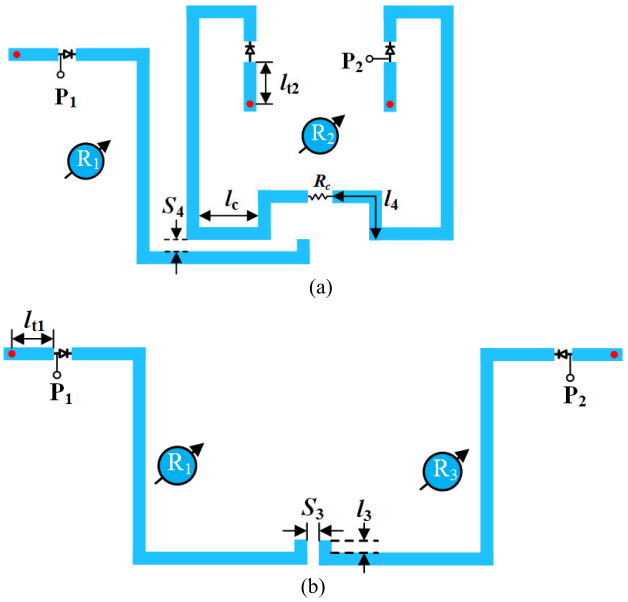

FIGURE 21. Circuit models for extracting (a) m_{12} and (b) m_{13} of the upper channel.

2) UPPER CHANNEL

The three-pole FA-BPF with the same CABW is shown in Fig. 20 to realize the upper channel in Fig. 9(a). It is observed that the filter is composed of two QWSTRs (R_1 and R_3) and one HWSTR (R_2) shown in Fig. 9(a). Note here, the physical layout of the feeding structure is designed compatible with both the lower and upper channels using the same feeding line. According to the design flow summarized before, the coupling coefficients and external quality of the upper channel are extracted and determined. The models for extracting m_{12} and m_{13} are shown in Fig. 21.

According to the predefined FTR, the length of the resonator and varactor-loading position are initiated. Based on the model shown in Fig. 21(a), the curves of the m_{12} are extracted and depicted in Fig. 22. The m_{12} can be designed as follow. First, choosing the proper value of l_c obtains the linear variation ofm_{12}. Then, changing S_4 shifts the m_{12} curve

TABLE 3. The initial and optimized physical dimensions of the upper channel (unit: mm).

	$W_0/W_1/W_2$	$S_1/S_2/S_3/S_4$	$l_1/\ l_2/\ l_3/\ l_4/\ l_5/$ $l_6/l_{t1}/l_{t2}/l_c$	D
Init.	2.4/2.2/0.72	0.3/2/0.4/0.3	27.5/27/0.6/5/3/ 4.9/5/5/3.2	0.4
Opt.	2.4/2.2/0.72	0.2/2/0.3/0.2	29.45/28.2/0.6/4.2/2/ 4.5/2.5/2.7/3.48	0.4

TABLE 4. The capacitance values and bias voltages for the upper channel.

Freq.(GHz)	C_{t1}(pF)	C_{t2}(pF)	V_{t1}(V)	V_{t2}(V)
1.9	10.3	15	1.6	0.0
2.45	1.58	1.54	7.9	7.4
3.0	0.65	0.6	20.2	23.2

position to the desired value with the fixed variation slope. Finally, changing l_4 yields the optimal m_{12} curve.

Based on the model shown in Fig. 21(b), the curves of the m_{13} are extracted in Fig. 23. Choosing the appropriate value of S_3 and l_3 can obtain almost constant m_{13} in EVCM. The source-load coupling m_{sl} can be achieved by choosing a proper S_2, which also predefines passband selectivity.

Based on the model shown in Fig. 24(a), the curves of Q_e are extracted and shown in Fig. 24(b) and (c). By choosing the appropriate values of l_6 and S_1 to determine the slope and the value range, the desired curve in EVCM can be realized.

Following the design procedure, the initial parameters are determined. The fine optimization process is implemented to improve CABW and RL performance. l_4 and l_5 are adjusted to obtain more stable CABW and adjust TZ position. l_{t1} and l_{t2} are optimized to acquire good RL over the entire FTR, which, however, leads to the shift of the FTR, m_{12} and m_{13}. l_1 and l_2 are slightly adjusted to correct FTR. Adjusting l_c and S_4 corrects m_{12}, and adjusting S_3 and l_3 corrects m_{13}. Through a few iterations of optimization, the desired filter performance is obtained. Table 3 compares the initial and optimized dimensions.

For verification, the filter is also fabricated and measured. The voltages V_{t1} from 0.6 V to 20.2 V and V_{t2} from 0.0 V to 23.2 V are applied to control the filter. The synthesized, simulated and measured frequency responses are shown in Fig. 25, where the bias resistor R_b is 100 kΩ and R_c is 30 Ω. As observed, the measured results agree well with the simulated results and also reasonably match the synthesized results. The minimum IL varies from 1.9 dB to 2.9 dB and the *FTR* is 1.9-3.0 GHz (44.9%). As the frequency is tuned, the ABW is kept constant at 194.5±2.5 MHz. Two TZs appeared in the lower stopband. Due to the second odd mode of HWSTR which is not completely suppressed, the TZ predefined at the upper stopband disappeared. The ABW and IL versus the tuning center frequency are presented in

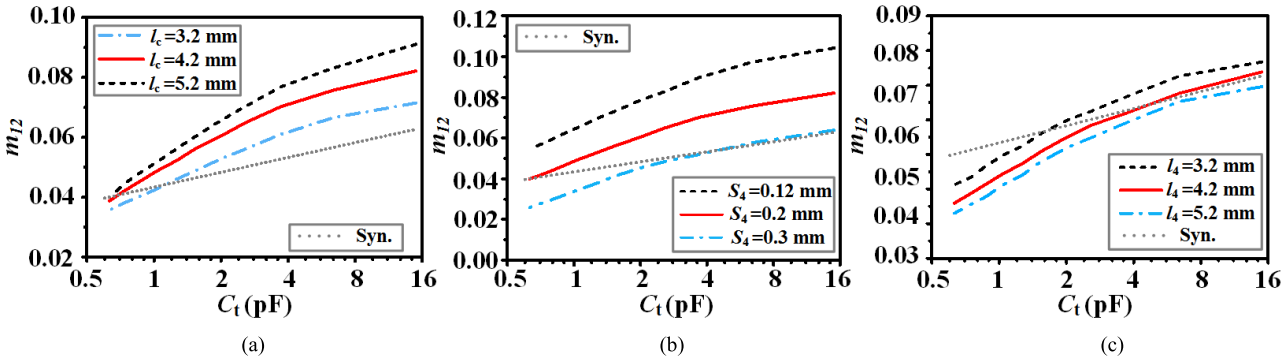

FIGURE 22. Coupling coefficient m12 versus Ct with different (a) lc when S4 = 0.3 mm, l4 = 4.2 mm, (b) S4 when lc = 4.2 mm and l4 = 4.2 mm, (c) l4 when lc = 4.2 mm, S4 = 0.3 mm.

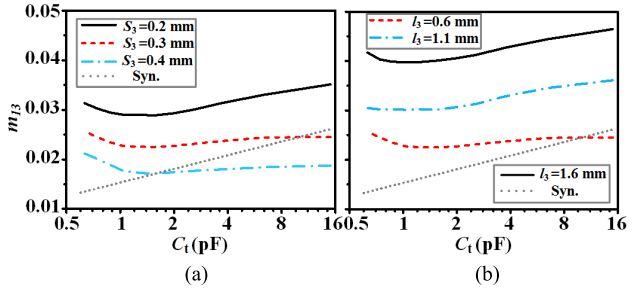

FIGURE 23. Coupling coefficient m_{13} versus C_t with different (a) S_3 when l_3 = 0.6 mm (b) l_3 when S_3 = 0.3 mm.

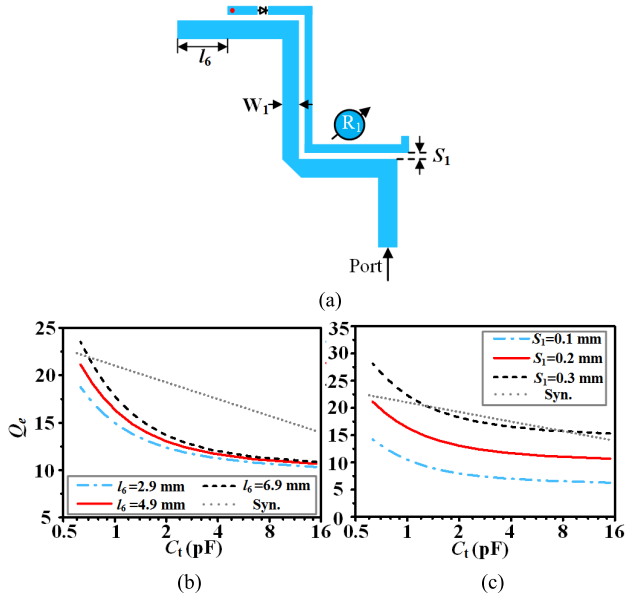

FIGURE 24. (a) Circuit model for extraction the Q_e of the upper channel. (b) Q_e versus C_t with different S_1 when l_6 = 4.9 mm. (c) Q_e versus C_t with different l_6 when S_1 = 0.2 mm. (W_1 = 2.2 mm).

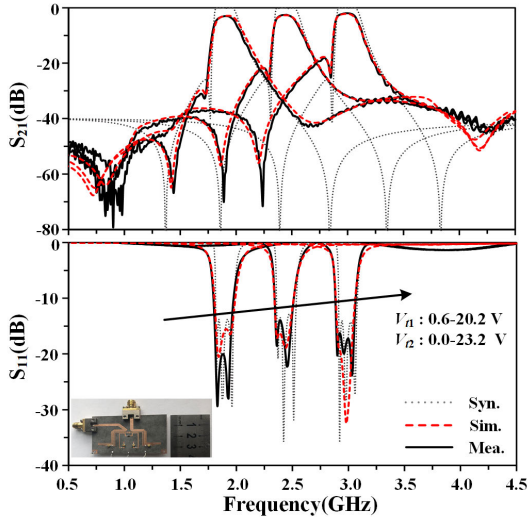

FIGURE 25. Synthesized, simulated and measured frequency responses of the upper channel with the photograph. (tanδ = 0.0009, R_S = 1 Ω).

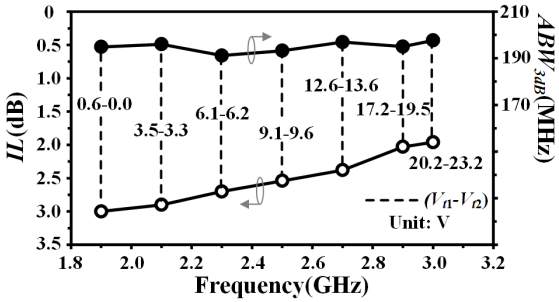

FIGURE 26. Measured IL and 3dB-bandwidth of the upper channel.

Fig. 26. The control voltages and corresponding capacitances are listed in Table 4.

E. DESIGN OF THREE-POLE FA-BPD WITH IC.CABW

By feeding the lower channel and upper channel with a common coupling line, the FA-BPD is formed as shown in Fig. 27. The dimensions of the FA-BPD for each channel are the same as two single-channel FA-BPFs'. Because two filters are loaded by the common feeding line, the mutual loading between two channels happens [24]. The external quality factors of two standalone filters are extracted and compared in Fig. 28 with and without the mutual loading effect, and also compared with theoretical curves. A slight

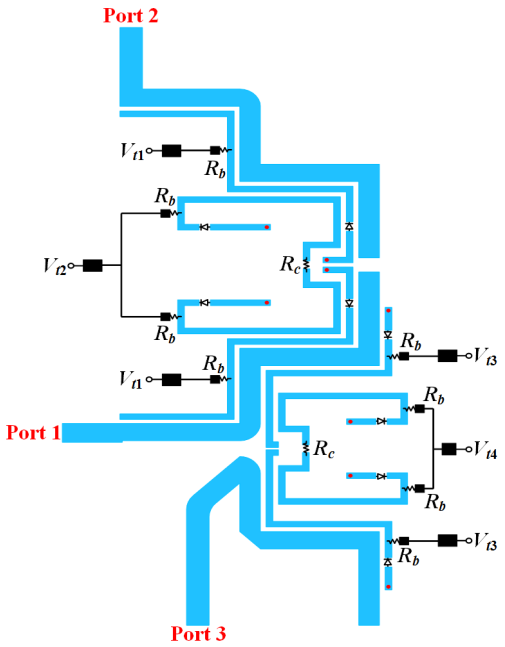

FIGURE 27. Layout of the proposed FA-BPD.

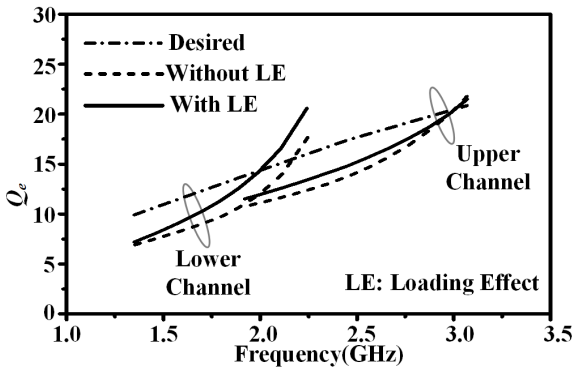

FIGURE 28. Extracted Q_e curves with and without the mutual loading, and the desired value for both channels of the diplexer.

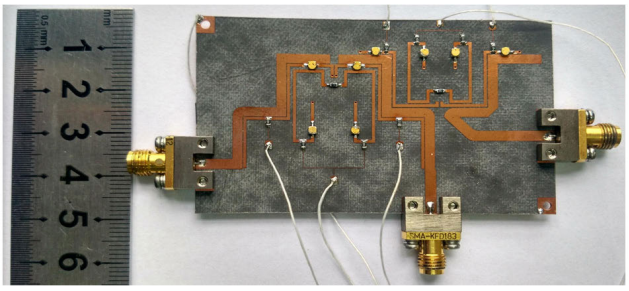

FIGURE 29. Photograph of the FA-BPD.

difference in the high-frequency area of the lower channel and in the lower-frequency area of the upper channel can be observed. However, the loading effect will not affect the predefined FTRs of the frequency-agile passbands and will only degrade the RL of the passbands within an acceptable level.

TABLE 5. The capacitance values and bias voltages for lower channel with upper channel fixed.

Freq.(GHz)	C_{t1}(pF)	C_{t2}(pF)	V_{t1}(V)	V_{t2}(V)
1.35	10.3	15	1.3	0.0
1.55	4	5	4.4	3.3
1.75	1.93	2	7.0	6.5
1.95	1.27	1.3	10.9	10.4
2.25	0.65	0.68	19.9	18.4

(V_{t3} = 21.7 V, V_{t4} = 23.3 V)

TABLE 6. The capacitance values and control voltages for upper channel with lower channel fixed.

Freq.(GHz)	C_{t3}(pF)	C_{t4}(pF)	V_{t3}(V)	V_{t4}(V)
1.9	9.7	15	1.1	0.0
2.0	5.7	6.4	2.2	1.8
2.2	2.58	2.58	4.9	4.6
2.4	1.59	1.54	7.7	7.6
2.6	1.09	1.03	11.0	11.3
2.8	0.79	0.74	15.5	16.3
3.0	0.65	0.6	18.9	19.4

(V_{t1} = 1.3 V, V_{t2} = 0 V)

For verification, the FA-BPD is fabricated and measured. The photograph is shown in Fig. 29. The resistors R_b and R_c (shown in Fig. 27) are 100 kΩ and 30 Ω, respectively. The control voltages areV_{t1}, V_{t2} for the lower channel and V_{t3}, V_{t4} for the upper channel.

The frequency responses of the FA-BPD are measured using the four-port Keysight VNA N5245B. The measured and simulated performance is presented in Fig. 30 where one channel is tuned and the other is fixed. As shown in Fig. 30(a), by changing V_{t1}, V_{t2} and fixing V_{t3}, V_{t4}, the center frequency of the lower passband is tuned from 1.35 to 2.25 GHz (the upper passband fixed at 3 GHz), while keeping the 3dB-bandwidth at 193±7 MHz and RL better than 10 dB. The measured IL varies from 2.2 dB to 2.7 dB and isolation level keeps better than 38 dB over the FTR. As shown in Fig. 30(b), by changing V_{t3}, V_{t4} and fixing V_{t1}, V_{t2} (lower passband fixed at 1.35 GHz), the center frequency of the upper passband is tuned from1.9 GHz to 3.0 GHz and the 3dB-bandwidth is 196±6 MHz, while the RL is maintained better than 13 dB. The measured IL is in the range of 2.1-3.3 dB and the isolation level keeps better than 45 dB for all of the tuning states. The bandwidths of the two channels exhibit almost constant and identical. It should be noted that the IL and bandwidth of two channels shows a little different when compared to those of the standalone single-band filters. This is probably because of the fabrication tolerance and the loading effect. Note that, due to the spurious mode, one of TZs of each channel disappears as channel center frequency is tuned. The capacitance values

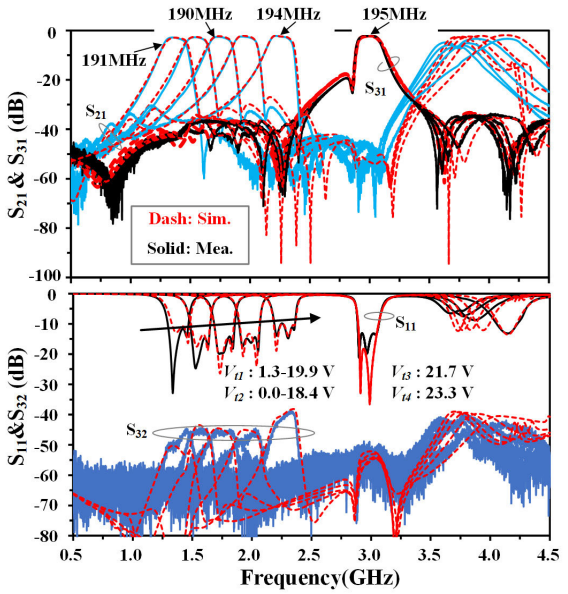

(a)

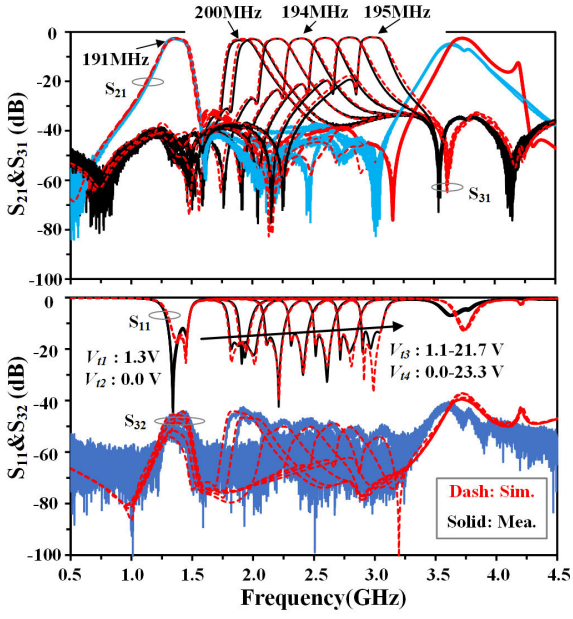

(b)

FIGURE 30. Measured and simulated results of the proposed FA-BPD. (a) Lower channel is tuned with upper channel fixed at 3 GHz. (b) The upper channel is tuned with a lower channel fixed at 1.35 GHz.

and the control voltages of the responses in Fig. 30(a) and (b) are given in Table 5 and 6.

For the application of some equal-BW reconfigurable FDD communication systems, two channels are required to be tuned synchronously with a specified frequency spacing. Two channels tuned synchronously with a frequency spacing of 500 MHz are measured and plotted in Fig. 31. As shown, the center frequencies of the lower and upper passbands are tuned from 1.4 to 2.2 GHz and from 1.9 GHz to 2.7 GHz.

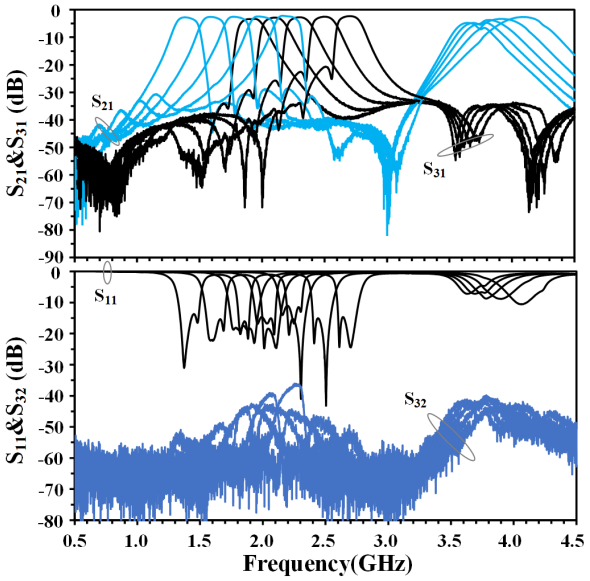

FIGURE 31. Tuning performance of the proposed FA-BPD with the constant frequency space of 500MHz when two channels are synchronously tuned.

TABLE 7. The capacitance values and control voltages for Synchronously-tuned two channels.

f_L (GHz)	V_{t1} (V)	V_{t2} (V)	f_U (GHz)	V_{t3} (V)	V_{t4} (V)
1.4	1.9	0.8	1.9	0.6	0.0
1.6	4.6	4.1	2.1	3.5	3.3
1.8	7.9	7.4	2.3	6.1	6.2
2.0	11.1	11	2.5	9.1	9.6
2.2	18.8	17	2.7	12.6	13.6

f_L: Lower channel frequency; f_U : Upper channel frequency.

Two-channel responses are almost the same as they are tuned separately. The control voltages for the measured frequency responses are listed in Table 7.

The power handling capacity and nonlinearity are important for practical application. Using the four-port Keysight VNA N5245B, the power handling ability of the proposed FA-BPD is measured with three different levels of input power. As shown in Fig. 32, the frequency response starts to distort when the input power level is above 12 dBm, indicating that the FA-BPD can handle at least 10 dBm input power level without distortion.

The linearity test setup is built up as shown in Fig. 33 to measure the third-order intermodulation intercept point (IIP3) [19]. Two signal generators E4438C and E8251A, power divider 11667B and spectrum analyzer N9010A all from Keysight Technologies are utilized. The IIP3 is measured by using a two-tone signal with a frequency spacing of 1MHz. The measured IIP3 varies from 22 dBm to 28 dBm,

TABLE 8. Performance comparisons between reported varactor-tuned FA-BPD and this work.

REF		FTR (GHz&%)	ST FTR (MHz)	Or.	IL (dB)	RL (dB)	Num. of TZ	Equal BW	C. A/FBW (MHz)	Num. of Var.	Num. of bias	Isolation level $\|S_{32}\|$(dB)	Design /control	Area $(\lambda_g \times \lambda_g)^1$
[3]	L. C. U. C	1.43-2.07(37.3%) 1.53-2.27 (39%)	640	3	<7.7	>8	0	FBW	~4.8% -	9	5	>22	complex	0.13×0.28
[4]	L. C. U. C	1.28-1.78(32.7%) 2-2.3 (13%)	300	3	<8.2	>10	1 1	No	No	14	6	>35	complex	0.39×0.64
[5]	L. C. U. C	1.2-1.8 (35%) 2.0-2.6 (26.1%)	600	4	<8.5	>10	1 2	No	4.5±0.5% - 5.5±0.5% -	8	8	>35	simple	0.28×0.46
[6]	L. C. U. C	0.94-1.21(25.1%) 1.51-1.91(23.5%)	270	3	<2.9	≈15	1 1	No	60-90 - 120-160 -	15	12	>51	complex	0.11×0.12
[7]	L. C. U. C	0.54-0.94(53.9%) 1.06-1.69(46.2%)	400	3	<7.72	>15	0	No	No 10.5±0.2%*	16	6	>44	complex	0.07×0.04
[8]	L. C. U. C	0.72-1.05(38%) 1.22-1.72(34%)	330	3	<4.9	>10	3 3	No	6.45±0.5%- ~4.8%-	11	2	>39	simple	0.1×0.1
[9]	L. C. U. C	1.05-1.35 (25%) 1.3-1.6 (20.7%)	300	4	<3.6	>10	4 4	ABW	133.5±2.5*	8	4	>36	simple	0.55×0.63
This work	L. C U. C	1.35-2.25(50%) 1.9-3.0(44.9%)	900	3	<3.3	>11	3 3	ABW	194±8*	8	4	>38	simple	0.42×0.19

L. C: Lower channel; U. C: Upper channel; Or.: Order; ST FTR: FTR when two channels are tuned synchronously. *: 3dB BW; -: 1 dB BW.
λ_g: The guided wavelength evaluated at the lowest frequency of the lower channel.

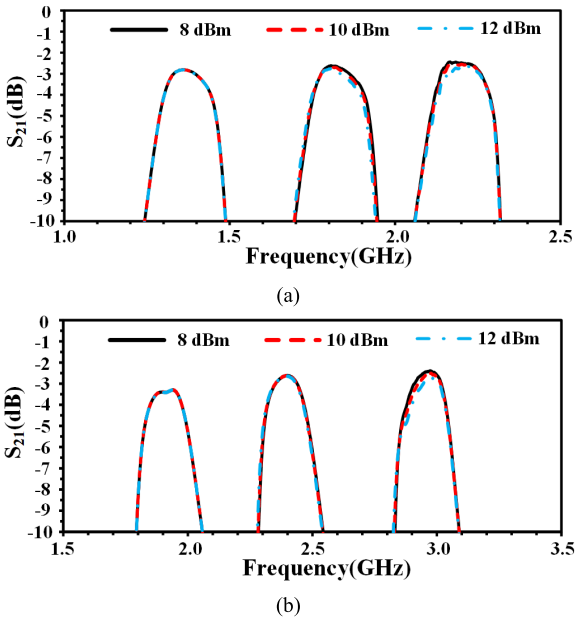

FIGURE 32. Frequency responses of the FA-BPD under input power level of 8 dBm, 10 dBm, 12 dBm, (a) for lower channel and (b) for the upper channel.

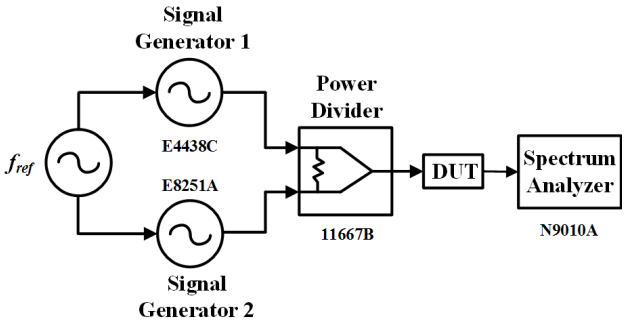

FIGURE 33. IIP3 measurement setup for the proposed FA-BPD.

and 21.1 dBm to 24.7 dBm respectively for lower and upper channel.

Performance comparisons between the other high-performance tunable diplexers and the proposed FA-BPD are listed in Table 8. The proposed FA-BPD achieves IC.ABW. Relatively wider FTR is also achieved. Besides, the FA-BPD operating at a higher frequency band exhibits lower IL (< 3.3 dB) over the entire FTR. The number of employed varactors and biases are just 8 and 4, which indicates that the control process of the proposed FA-BPD is easier than the other three-pole tunable diplexers. Because of two TZs appearing on the passband of the other channel, the isolation level achieves better than 38 dB without adding any extra matching network or introducing more loss.

III. CONCLUSION

In this paper, a 1.35-2.25/1.9-3 GHz FA-BPD with IC.ABW and good isolation is implemented. Based on EVCM synthesis, two three-pole FA-BPFs with three TZs, mirror-symmetric TZ distributions, and identical CABW are designed individually. By feeding the two FA-BPFs with a common coupling feed-line directly, a 1.35-3-GHz three-pole FA-BPD is realized. The proposed FA-BPD controlled in a simple way exhibits the same bandwidth between two channels. In comparison with the other reported FA-BPDs, the better isolation level and lower IL over the entire FTR are achieved. The measurement results agree well with the simulated results, which validate superiority of the proposed diplexer.

REFERENCES

[1] R. Eslampanah, S. Ahmed, M. Williamson, J.-M. Redouté, and M. Faulkner, "Adaptive duplexing for transceivers supporting aggregated transmissions," *IEEE Trans. Veh. Technol.*, vol. 65, no. 9, pp. 6842–6852, Sep. 2016.

[2] D. L. Kaczman, M. Shah, N. Godambe, M. Alam, H. Guimaraes, and L. M. Han, "A single-chip tri-band (2100, 1900, 850/800 MHz) WCDMA/HSDPA cellular transceiver," *IEEE J. Solid-State Circuits*, vol. 41, no. 5, pp. 1122–1132, May 2006.
[3] C. H. Ko and G. M. Rebeiz, "A 1.4–2.3-GHz tunable diplexer based on reconfigurable matching networks," *IEEE Trans. Microw. Theory Techn.*, vol. 63, no. 5, pp. 1595–1602, May 2015.
[4] T. Yang and G. M. Rebeiz, "Three-pole 1.3–2.4-GHz diplexer and 1.1–2.45-GHz dual-band filter with common resonator topology and flexible tuning capabilities," *IEEE Trans. Microw. Theory Techn.*, vol. 61, no. 10, pp. 3613–3624, Oct. 2013.
[5] T. Yang and G. M. Rebeiz, "A simple and effective method for 1.9–3.4-GHz tunable diplexer with compact size and constant fractional bandwidth," *IEEE Trans. Microw. Theory Techn.*, vol. 64, no. 2, pp. 436–449, Feb. 2016.
[6] P. L. Chi and T. Yang, "Three-pole reconfigurable 0.94–1.91-GHz diplexer with bandwidth and transmission zero control," *IEEE Trans. Microw. Theory Techn.*, vol. 65, no. 1, pp. 96–108, Jan. 2017.
[7] J. Xu and Y. Zhu, "Tunable bandpass filter using switched tunable diplexer technique," *IEEE Trans. Ind. Electron.*, vol. 64, no. 4, pp. 3118–3126, Apr. 2017.
[8] L. Gao, T.-W. Lin, and G. M. Rebeiz, "Tunable three-Pole diplexer with high selectivity and isolation," in *IEEE MTT-S Int. Microw. Symp. Dig.*, Philadelphia, PA, USA, Jun. 2018, pp. 1378–1380.
[9] D. Lu, M. Yu, N. S. Barker, Z. Li, W. Li, and X. Tang, "Advanced synthesis of wide-tuning-range frequency-adaptive bandpass filter with constant-absolute bandwidth," *IEEE Trans. Microw. Theory Techn.*, to be published.
[10] S. J. Park and G. M. Rebeiz, "Low-loss two-pole tunable filters with three different predefined bandwidth characteristics," *IEEE Trans. Microw. Theory Techn.*, vol. 56, no. 5, pp. 1137–1148, May 2008.
[11] X. Y. Zhang, Q. Xue, C. H. Chan, and B. J. Hu, "Low-loss frequency-agile bandpass filters with controllable bandwidth and suppressed second harmonic," *IEEE Trans. Microw. Theory Techn.*, vol. 58, no. 6, pp. 1557–1564, Jun. 2010.
[12] L. Athukorala and D. Budimir, "Compact second-order highly linear varactor-tuned dual-mode filters with constant bandwidth," *IEEE Trans. Microw. Theory Techn.*, vol. 59, no. 9, pp. 2214–2220, Sep. 2011.
[13] Y.-C. Chiou and G. M. Rebeiz, "A tunable three-pole 1.5–2.2-GHz bandpass filter with bandwidth and transmission zero control," *IEEE Trans. Microw. Theory Techn.*, vol. 59, no. 11, pp. 2872–2878, Nov. 2011.
[14] Y.-C. Chiou and G. M. Rebeiz, "A quasi elliptic function 1.75–2.25 GHz 3-pole bandpass filter with bandwidth control," *IEEE Trans. Microw. Theory Techn.*, vol. 60, no. 2, pp. 244–249, Feb. 2012.
[15] J.-R. Mao, W.-W. Choi, K.-W. Tam, W. Q. Che, and Q. Xue, "Tunable bandpass filter design based on external quality factor tuning and multiple mode resonators for wideband applications," *IEEE Trans. Microw. Theory Techn.*, vol. 61, no. 7, pp. 2574–2584, Jul. 2013.
[16] C. Ge and X.-W. Zhu, "Highly-selective tunable bandpass filter with two-path mixed coupling," *IEEE Microw. Wireless Compon. Lett.*, vol. 24, no. 7, pp. 451–453, Jul. 2014.
[17] Z. Zhao, J. Chen, L. Yang, and K. Chen, "Three-pole tunable filters with constant bandwidth using mixed combline and split-ring resonators," *IEEE Microw. Wireless Compon. Lett.*, vol. 24, no. 10, pp. 671–673, Oct. 2014.
[18] P.-L. Chi, T. Yang, and T.-Y. Tsai, "A fully tunable two-pole bandpass filter," *IEEE Microw. Wireless Compon. Lett.*, vol. 25, no. 5, pp. 292–294, May 2015.
[19] D. Lu, N. S. Barker, and X. Tang, "A simple frequency-agile bandpass filter with predefined bandwidth and stopband using synchronously tuned dual-mode resonator," *IEEE Microw. Compon. Lett.*, vol. 27, no. 11, pp. 983–985, Nov. 2017.
[20] C.-F. Chen, G.-Y. Wang, and J.-J. Li, "Microstrip switchable and fully tunable bandpass filter with continuous frequency tuning range," *IEEE Microw. Wireless Compon. Lett.*, vol. 28, no. 6, pp. 500–502, Jun. 2018.
[21] *M/A-COM MA46H202 Data Sheet*, M/A-COM, Lowell, MA, USA, 2006.
[22] J. Shi and Q. Xue, "Balanced bandpass filters using center-loaded half-wavelength resonators," *IEEE Trans. Microw. Theory Techn.*, vol. 58, no. 4, pp. 970–977, Apr. 2010.
[23] J.-S. Hong and M. J. Lancaster, *Microstrip Filters for RF/Microwave Applications*. New York, NY, USA: Wiley, 2001.
[24] C. Carceller, P. Soto, V. Boria, M. Guglielmi, and J. Gil, "Design of compact wideband manifold-coupled multiplexers," *IEEE Trans. Microw. Theory Techn.*, vol. 63, no. 10, pp. 3398–3407, Oct. 2015.

ZHIYOU LI was born in Luzhou, China, in 1990. He received the B.Eng. degree in electronic engineering from the University of Electronic Science and Technology of China, Chengdu, China, in 2014, where he is currently pursuing the Ph.D. degree.

XIAOHONG TANG (M'08) received the B.S. and Ph.D. degrees in electromagnetism and microwave technology from the University of Electronic Science and Technology of China (UESTC), where he is currently a Professor. He has authored more than 100 journal and conference papers. He was also a recipient of several national and provincial awards. His research interests include microwave and millimeter communication and computational electromagnetics.

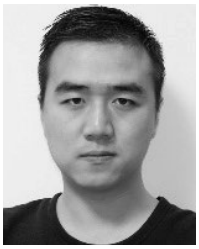

DI LU (S'14–M'18) received the M.S. degree from the Chengdu University of Information and Technology, in 2013, and the Ph.D. degree from the University of Science and Technology of China (UESTC), in 2018.

From 2015 to 2017, he was a Visiting Staff with the University of Virginia, Charlottesville, VA, USA. He is currently a Postdoctoral Researcher with the Chinese University of Hong Kong, Hong Kong. His main research interests include design of MMIC microwave passive circuit, tunable circuit, frequency multipliers, mixers, millimeter-wave circuits, and RF MEMS.

ZONGQI CAI was born in Fujian, China, in 1991. He received the B.S. degree from Jimei University, Fujian, China, in 2013. He is currently pursuing the Ph.D. degree with the University of Electronic Science and Technology of China, Chengdu.

Since 2017, he has been a Visiting Student at the University of Technology Sydney. His current research interests include RF/microwave planar oscillators and VCOs, tunable filters and duplexers, and microwave and millimeter Doppler sensors.

YONG LIU received the B.S. and Ph.D. degrees in electromagnetism and microwave technology from the University of Electronic Science and Technology of China (UESTC), where he is currently a Research Associate. He has authored more than 15 journal and conference papers. His research interests include microwave and millimeter-wave communication and circuit system design.

JUNXIN LUO received the M.Eng. degree in electronic science and technology from the University of Electronic Science and Technology of China, Chengdu, China, in 2012. His current research interests include microwave and millimeter-wave wireless communication systems.